STEM Imaging with Beam-Induced Hole and Secondary Electron Currents

William A. Hubbard,[1,2] Matthew Mecklenburg,[3] Ho Leung Chan,[1,2] and B. C. Regan[1,2,*]

[1]*Department of Physics and Astronomy, University of California, Los Angeles, California 90095, USA*

[2]*California NanoSystems Institute, University of California, Los Angeles, California 90095, USA*

[3]*Core Center of Excellence in Nano Imaging, University of Southern California, Los Angeles, California 90089, USA*

In standard electron-beam-induced-current (EBIC) imaging, the scanning electron beam creates electron-hole pairs that are separated by an in-sample electric field, producing a current in the sample. In standard scanning electron microscopy (SEM), the scanning electron beam ejects secondary electrons (SEs), which are detected away from the sample. While a beam electron in a scanning transmission electron microscope (STEM) can produce many electron-hole pairs, the yield of SEs is only a few percent for beam energies in the range 60–300 keV, making the latter signal much more difficult to detect on sample as an EBIC. Here we show that the on-sample EBIC in a STEM registers both SE emission and SE capture as holes and electrons, respectively. Detecting both charge carriers produces differential image contrast not accessible with standard, off-sample SE imaging. In a double EBIC-imaging configuration incorporating two current amplifiers, both charge carriers can even be captured simultaneously. Compared with the current produced in standard EBIC imaging, which highlights only the regions in a sample that contain electric fields, the EBIC produced by SE emission, or SEEBIC, is small (picoampere scale). But SEEBIC imaging can produce contrast anywhere in a sample, exposing the texture of buried interfaces, connectivity, and other electronic properties of interest in nanoelectronic devices, even in metals and other structures without internal electric fields.

I. INTRODUCTION

Transmission electron microscopy (TEM) is a powerful, high-resolution technique that can be applied to study functioning nanoelectronic systems *in situ*. Conventional TEM excels at determining the physical structure of the sample, namely the position and identity of the sample's constituent atoms. While this (physical) structure dictates many of the sample's properties, in devices it frequently is only of secondary interest. A device's function is often determined by its electronic, optical [1], or thermal [2] structure, to which conventional TEM is not directly sensitive.

In electron-beam-induced-current (EBIC) imaging, a focused electron beam is scanned across a sample that is attached to a transimpedance amplifier (TIA). Associating the measured sample current with the beam position forms the EBIC image [3,4]. EBIC imaging has been used extensively to map electric fields that are intrinsic to the sample, such as those in Si-dislocation defects [5–7] and in solar cells [8–12], and related properties, such as carrier lifetimes, diffusion lengths, defect energy levels, and surface recombination velocities [4,13]. In these experiments, a local electric field generates the EBIC by separating electron-hole pairs produced by the primary beam. Because one primary electron can create thousands of electron-hole pairs [14,15], this process has gain and the resulting signals are relatively large. Most EBIC studies have been conducted in a scanning electron microscope (SEM) [4,6]. EBIC imaging for the purpose of mapping electric fields has also been extended to scanning TEM (STEM), where TEM's better electron optics and electron-transparent samples both contribute to improved spatial resolution [11,16–19].

Here we demonstrate that STEM EBIC is sensitive to secondary electron (SE) emission, a much smaller signal distinct from the conventional electric-field-related and beam-absorption-related EBIC signals. SEs are electrons ejected from the sample by interactions with the primary beam. We generate images where the contrast is dominated by SE emission and capture. Use of a "double EBIC"-imaging configuration, where two neighboring electrodes are connected to separate TIAs, allows us to collect, separately, both some of the emitted SEs and all of the holes left behind. Unlike conventional TEM, secondary-electron-emission EBIC (SEEBIC) imaging—and especially STEM

————————
*regan@physics.ucla.edu

SEEBIC imaging—is directly sensitive to electronic properties; it can be used to assess connectivity and conductivity, and shows promise for mapping work function. Much of STEM SEEBIC imaging's revelatory strength derives from its ability to directly detect holes, which is impossible for an off-sample SE detector.

II. THEORY

We consider a region on the sample that, if insulating, might be scarcely larger than the probe size, but if conducting encompasses the full extent of the electrically connected area. When the microscope's electron beam is incident on this region, we approximate the steady-state current balance with [20,21]

$$I_B + I_{\text{in}} = I_T + I_A + I_{\text{BS}} + I_{\text{SE}} + V_S/R_S + I_{\text{out}}, \quad (1)$$

where I_B is the incident primary-beam current, I_T is the transmitted beam current, I_A is the absorbed beam current, I_{BS} is the backscattered current, I_{SE} is the secondary-electron current, and V_S and R_S are the sample potential (due to beam-induced charging, for instance) and effective resistance to ground, respectively. I_{in} and I_{out} represent on-sample device currents that can be controlled and/or measured, perhaps in the absence of the electron beam. In this paper we consider only bare electrodes where one end of the "device" is floating, in which case $I_{\text{in}} = 0$.

Very generally, the secondary-electron signal is easiest to detect in devices configured to be floating, or nearly so (i.e., with an effective device impedance $R \gtrsim 10$ MΩ, and preferably $\gg 1$ GΩ). Otherwise the SE current I_{SE} is obscured by the Johnson noise current $\delta I = \sqrt{4k_B T B/R}$, where $k_B T$ is the thermal energy and B is the amplifier bandwidth. For this reason, one might also take SEEBIC to stand for "single-ended EBIC." Standard electric-field-based EBIC, in contrast, requires a low-impedance connection to the side of the device opposite the TIA to prevent charging.

In TEM generally, and in the cases of interest here, the largest term on the right-hand side of Eq. (1) is $I_T \simeq I_B$, while I_A and I_{BS} are mostly negligible [20–22]. In SEM, where instead typically $I_T = 0$, $I_A \simeq I_B$ is a large background that makes observing the smaller I_{SE} via EBIC difficult. In an electrically isolated area, SE emission leads to charging [20] and $I_{\text{SE}} = -V_S/R_S$. If instead there is a low-impedance path to ground, or a virtual ground consisting of the input to a TIA, little charging occurs and a current $I_{\text{out}} = -I_{\text{SE}}$ is generated. In other words, a positive hole current flows into the amplifier that is equal and opposite to the negative SE current leaving the sample. For the TIA case, I_{out} provides the SEEBIC signal, which can be mapped pixel by pixel, as the beam scans the sample, to produce an image (Fig. 1).

The SE current detected depends on four multiplicative factors [22,23]. First, the rate of secondary generation is
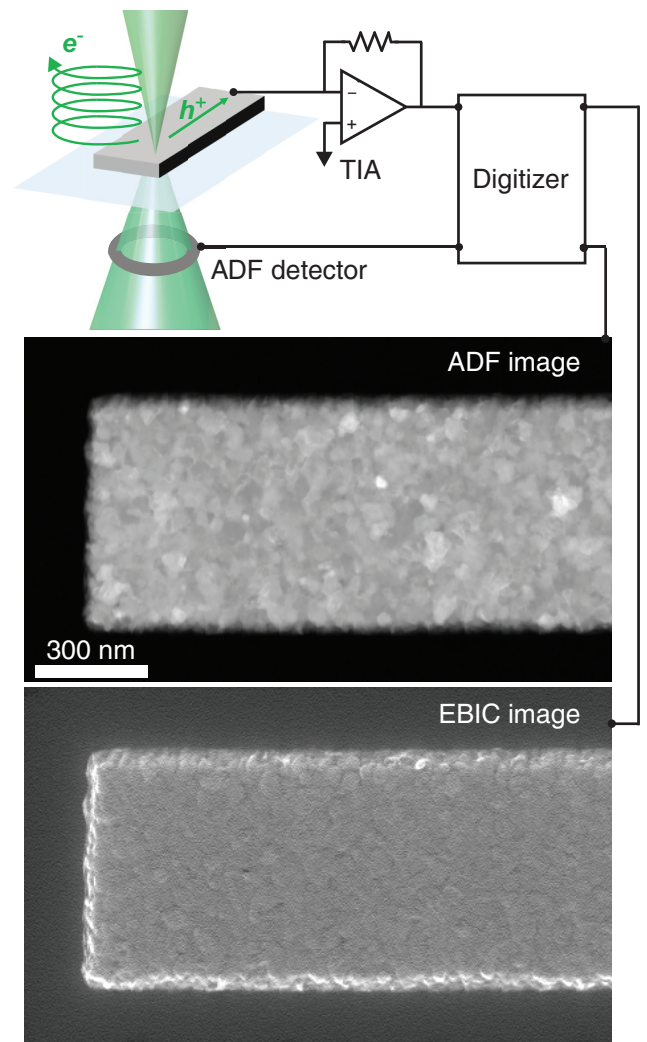

FIG. 1.   STEM SEEBIC imaging of a metal electrode. (top) A cartoon representation of the basic setup shows the electron beam rastering over a bare Al electrode. Scattered electrons produce the usual ADF image (middle). SEs ejected from the electrode leave holes behind, producing a positive current and corresponding bright contrast in the EBIC image (bottom). The imaged electrode is maintained at virtual ground by the TIA.

determined by the primary-beam energy E_B, the beam current I_B, and properties of the irradiated material. Second, the fraction of these secondaries that make it to the sample surface is determined by their mean free path (MFP) and distance to the surface. Third, the work function Φ_W (or the electron affinity χ for insulators) and surface potential V_S determine the escape probability once they are at the surface. Finally, the fraction of the escaped electrons that are counted by the detector depends on the efficiency and geometry of the detection apparatus, including the local electric and magnetic fields.

While calculating any of these factors is usually nontrivial, the SEEBIC case described above, where the beam is incident on a conductor connected to the TIA [see Eq. (1)],

contains an exception: the fourth factor is unity. In other words, the electrode struck by the beam functions as an SE detector with perfect detection efficiency (to within a sign). The net hole current (see Ref. [21] for a detailed discussion) is detected by the TIA, unlike the case for an off-sample SE detector, where some SEs might hit the detector and some might not.

To account for the physics underpinning the first and third factors, we adopt the following approximate expression [15,24] describing the scaling of I_{SE}:

$$I_{SE} \propto \frac{I_B}{E_B} \int_{eV_S}^{\infty} \frac{E_{SE} \, dE_{SE}}{(E_{SE} + \Phi_W)^4}$$
$$= \frac{I_B}{E_B} \times \frac{3eV_S + \Phi_W}{6(eV_S + \Phi_W)^3} \quad \text{for } eV_S \geq 0. \quad (2)$$

Here E_{SE} is the SE energy relative to the vacuum zero level. Only electrons with $E_{SE} > 0$ can escape.

The integral in Eq. (2) is most appropriate in the nonrelativistic limit, and more careful analyses based on Bethe's relativistic stopping-power relation [15,25] or dielectric theory [25] give I_{SE} scaling that is weaker than $1/E_B$. However, this simpler expression, commonly used to describe SEs in SEM [15], is sufficient for our modest quantitative purposes.

In place of the usual integration limit of 50 eV, the conventional upper energy limit for secondary electrons [15], we use infinity in Eq. (2). This substitution simplifies the result and introduces only a small error (approximately 3%). Note, however, that unity-detection-efficiency EBIC is fundamentally insensitive to backscattered electrons (where the charge originates in the primary beam, not in the sample), and cannot distinguish between Auger electrons and SEs. Furthermore, the number of high-energy SEs increases with increasing primary-electron energy [26], and our STEM accelerating voltages are high (80–300 kV) compared with the usual SEM EBIC case. Thus, this substitution also has several physical motivations.

With regard to the second of the four multiplicative factors mentioned above, the MFP for a SE in a material depends on the SE energy and the electron density of the material [24]. In general, the SE MFP is shorter in materials with higher conductivity [24], with metals and insulators having SE MFPs of a few nanometers and tens of nanometers, respectively [27,28]. Because of the shortness of the MFPs, SEEBIC imaging tends to be more sensitive to the sample's surface, as opposed to its bulk, than conventional TEM imaging modes.

III. EXPERIMENTAL DETAILS

Silicon wafers 200 μm thick and coated with 800 nm of SiO$_2$ and 20 nm of Si$_3$N$_4$ are selectively etched with KOH to reveal SiO$_2$/Si$_3$N$_4$ membranes on which

Ti(5 nm)/Pt(25 nm) electrodes are patterned optically. (This slash notation lists materials in the order in which they are deposited, here indicating a 5-nm titanium adhesion layer covered with 25 nm of platinum.) These substrates are patterned with additional features via electron-beam lithography, and then the supporting oxide is removed with an HF-vapor etch (leaving the nitride) to make the samples electron transparent. Unless otherwise noted, all imaging is done in an FEI Titan 80-300 S/TEM with an 80-kV accelerating voltage and a beam current of approximately 30 pA, as measured with a Faraday cup [21]. A TIA (FEMTO DLPCA-200), connected to the sample via a biasing holder (Hummingbird Scientific), converts the EBIC into a voltage signal that is digitized along with the STEM detector signals [18]. In some cases, two TIAs connected to two different electrodes on the sample are used to simultaneously generate two EBIC images (double EBIC imaging). The EBIC scans presented here are 256×256 pixels, and are acquired with a dwell time of approximately 2.5 ms at each pixel (3 min/frame). No filtering (e.g., for 60-Hz noise) is applied to any of the images.

IV. RESULTS AND DISCUSSION

We first illustrate the basics of SEEBIC imaging with a simple example, showing images of a single bare 100-nm-thick aluminum electrode on a Si$_3$N$_4$(15 nm)/ Al$_2$O$_3$(15 nm) membrane (Fig. 1). As indicated in the cartoon at the top of Fig. 1, as the focused electron beam rasters over the sample, several signals are digitized in parallel: the signals from the usual STEM detectors, and the EBIC signal. Here just the annular dark field (ADF) is shown (middle of Fig. 1) together with the EBIC image (bottom of Fig. 1). The EBIC image shows contrast that is unlike, for example, that of the ADF image, and is very similar to that of an SE image acquired in a SEM [21], which already points to SEs as the source of the contrast. For instance, the electrode edges appear markedly brighter in the EBIC image (and not in the ADF image), exhibiting the enhanced emission that gives the well-known edge contrast of SE imaging [15].

To further implicate SEs, we use double EBIC imaging, connecting separate TIAs to two separated, bare electrodes on a Si$_3$N$_4$ membrane (Fig. 2). In each of the conventional STEM images, the two Ti(5 nm)/Pt(25 nm) electrodes give identical contrast: primarily dark in the bright-field (BF) detector [Fig. 2(a)], and primarily bright in the ADF detector [Fig. 2(b)], with small variations due to different grain orientations in the polycrystalline metal. In the two STEM EBIC images [Figs. 2(c) and 2(d)], however, the electrode contrast flips depending on whether the TIA generating the image is connected to the electrode being imaged or not.

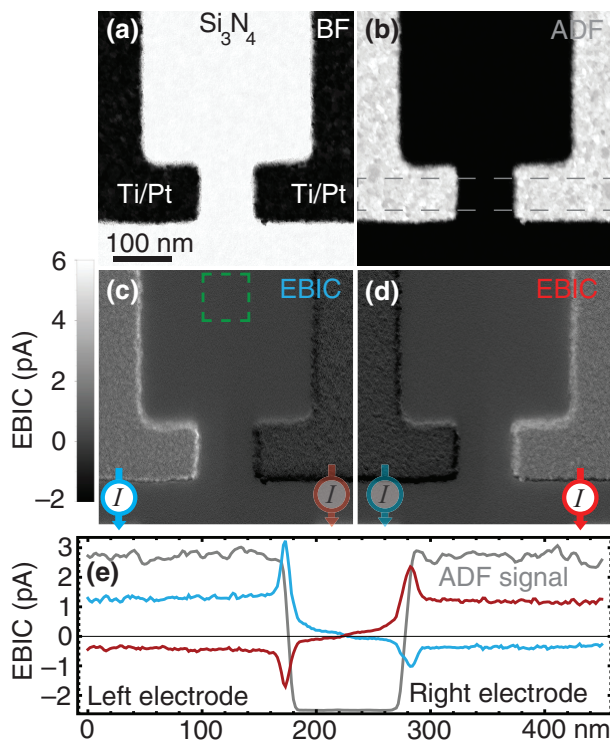This contrast reversal is expected for SEEBIC imaging. SEs emitted from an electrode connected directly to

FIG. 2. Conventional STEM and double STEM SEEBIC imaging of Ti/Pt electrodes. The simultaneously acquired (a) BF, (b) ADF, and (c),(d) STEM EBIC images show Ti(5 nm)/Pt(25 nm) electrodes on a Si_3N_4 membrane. TIAs are connected to the electrodes as indicated by the blue and red symbols in the STEM EBIC images, with the symbol shown as opaque in the image generated by that TIA. Bright (dark) contrast corresponds to positive (negative) current, as indicated by the current scale for (c) and (d) that is to the left of (c). The gray, blue, and red plots in (e) show line profiles from (b)–(d) taken in the region indicated by the gray rectangle in (b). The gray plot is in arbitrary units and the blue and red plots use the scale on the y axis. The images in (a)–(d) are rotated 90° counterclockwise, so that the fast scan direction is bottom to top. EBIC values in (c),(d) are given relative to their respective averages from the region outlined in green in (c).

the TIA generate positive current via the holes that are left behind. SEs emitted from elsewhere in the sample (e.g., the opposing electrode) can also be captured by the electrode connected to the TIA, and generate a corresponding negative current [21]. [Replacing, for instance, the red TIA connected to the right electrode in Fig. 2 with a ground connection would mean that the image in Fig. 2(d) was not acquired, but the image in Fig. 2(c) would be unchanged.] As explained earlier, the connected electrode functions as a SE-emission detector with unit efficiency. Since the beam-electrode interaction physics is independent of the electrode-TIA connections, with two amplifiers (or two sequential measurements on different electrodes) we can calibrate the efficiency of SE capture precisely. Here the direct electrode captures a surprisingly [21] large

20%–50%, depending on the emission location, of the SEs emitted from the opposing electrode [Fig. 2(e)]. As seen in the EBIC images [Figs. 2(c) and 2(d)] and the line profiles [Fig. 2(e)], both the efficiency of SE generation and emission and the efficiency of SE capture are evidently enhanced at the electrode edges (again exhibiting the expected SE edge-contrast effect), while these efficiencies are comparatively uniform within an electrode. Note that were double EBIC imaging to be used in standard, electric-field-based EBIC, the electron and hole currents would have identical magnitudes [21]. Thus, having an electron current that is smaller than the hole current also supports the SE hypothesis.

The EBIC signals from the membrane show a subtle but unmistakable step at the midpoint between the electrodes, visible (all the way from top to bottom) in the images [Figs. 2(c) and 2(d)] and the plot [Fig. 2(e)]. This step indicates that the membrane has some conductivity: a hole created by SE emission is attracted to its image charge (there are no intrinsic or externally applied electric fields) and heads to the nearest electrode (or, more precisely, takes the least-resistive path toward ground), regardless of whether the interelectrode gap is small or not. With an off-sample SE detector [23], such differential contrast is unavailable; both electrodes give the same contrast (as in the BF and ADF images), and there is no dividing line. A hole cannot fly through a vacuum to be counted in an off-sample detector. Only the SE is detected—the fate of the corresponding hole, which remains in the sample, is unknown. SEEBIC imaging, on the other hand, detects the hole, and is sensitive to the sample properties not just at the SE ejection point but around it too. Thus, it can precisely locate the boundary of the conductance "watershed," even without the second SEEBIC image (i.e., double EBIC imaging is not necessary—a single image with one TIA is sufficient). In the device in Fig. 2, the lithography is nearly perfect, but in other cases [21] SEEBIC imaging reveals a nontrivial boundary that is not along the axis of symmetry.

For bare electrode devices the EBIC signal responds to changes in the primary-beam current and accelerating voltage as expected for SE emission [see Eq. (2)]. For Ti(5 nm)/Pt(25 nm) and 100-nm Al electrodes, the SEEBICs are linear in the incident-beam current (as measured with a Faraday cup [21]) at 80, 200, and 300 kV [Fig. 3(a)]. The slopes of these lines give the SE yield (i.e., the number of SEs per primary electron), and are in the range 0.5%–3%. The SE yield for each electrode material is inversely proportional to the primary beam energy [Fig. 3(b)], in agreement with Eq. (2). With only three data points for each of the two electrode materials, neither of which is freely suspended, we do not attempt to more precisely determine the power-law exponent.

We have described edge contrast, contrast reversal between EBIC electrodes, material-dependent yields, $I_{SE} \propto I_B$, and $I_{SE} \propto E_B^{-1}$. Varying the EBIC electrode
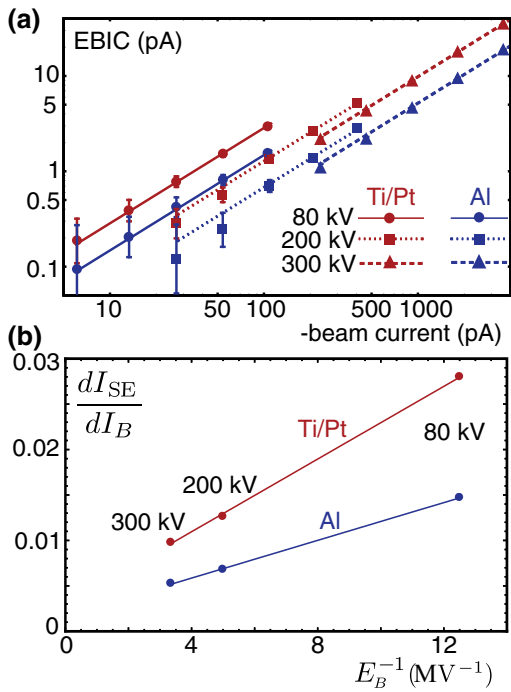
FIG. 3. EBIC vs beam current and SE yield vs inverse beam energy. In the plot (a), the EBIC current from Ti(5 nm)/Pt(25 nm) and 100-nm Al electrodes is shown (with fits to $I_{SE} = \delta \times I_B$) for five different beam currents I_B at each accelerating voltage of 80, 200, and 300 kV. The EBIC uncertainty is taken to be 0.1 pA. In the plot (b), the SE yield δ for each material, determined from the six fits in the plot (a), is linear in E_B^{-1}, as predicted by Eq. (2).

potential relative to ground (Fig. 4) further identifies SEs as the source of these signals, and also indicates that SEEBIC imaging might be used to map material work functions. Biasing the TIA's input relative to ground, we see that positive (negative) bias decreases (increases) the EBIC signal, demonstrating active SE voltage contrast without an off-sample detector [19]. Similar analysis of the conventional STEM signals shows no bias dependence.

For positive electrode bias voltages, the measured EBIC scales according to the dependence given in Eq. (2), and indicates that about 60% of the SEs have $E_{SE} < 9$ eV. Fitting the data (Fig. 4) yields agreement with previously measured values for the work functions of Al and Pt [29]. Interestingly, we find that subsequent EBIC images of the same region give work-function fit values that are systematically larger. For negative electrode bias voltages, we find that the SE yield increases as the bias magnitude increases. Both the increasing work functions and the increasing (as opposed to constant) yields with negative bias can be attributed to surface contamination [30]. SE emission is extremely sensitive to the presence of surface contaminants, even at monolayer thicknesses [31]. Imaging a sample in a merely high-vacuum (10^{-6}–10^{-3}-Pa) environment, such as exists in our microscope, is likely to alter the surface contamination layer. With an
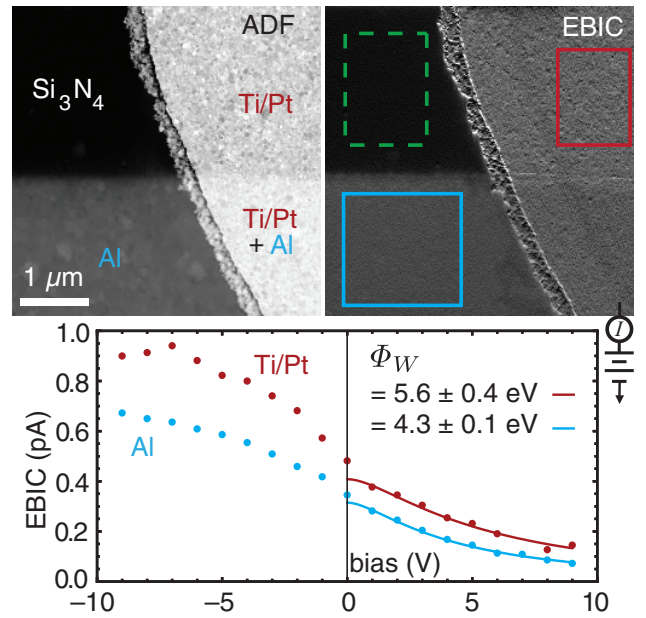

FIG. 4. ADF and EBIC images of Ti/Pt and Al electrodes and average SEEBIC from each material vs electrode bias. The images show four different material combinations: the bare Si_3N_4 membrane, Ti(5 nm)/Pt(25 nm), 100-nm Al, and Ti(5 nm)/Pt(25 nm)/Al(100 nm). The plot shows the average signal in the SEEBIC image measured on Al (blue box) and Ti/Pt (red box), with the average current measured on Si_3N_4 (green box) subtracted, for each bias value. The solid lines are fits to the SE-emission-current equation [Eq. (2)] for $V > 0$, with the work functions and zero-bias currents as free parameters.

ultrahigh-vacuum sample environment, however, the work function could be mapped quantitatively at high resolution by STEM SEEBIC imaging.

For a variety of materials the SEEBIC signal is thickness independent, at least for samples thinner than 100 nm, as expected for a surface-sensitive contrast mechanism [21]. Surprisingly, however, SEEBIC images can also show contrast based on buried surface texture. For instance, conventional STEM imaging of a Ti(5 nm)/Pt(25 nm) electrode shows grains with characteristic lateral dimensions
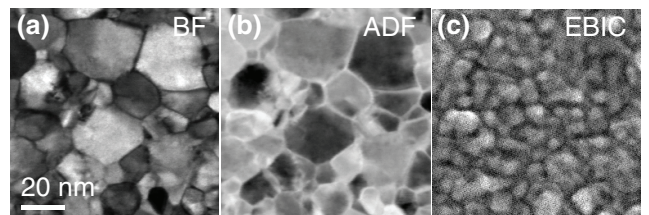

FIG. 5. Conventional STEM and STEM SEEBIC images of metallic grains in a Ti/Pt film. Simultaneously acquired BF (a), ADF (b), and EBIC (c) images of a Ti(5 nm)/Pt(25 nm) electrode on a Si_3N_4 membrane.

of about 25 nm [Figs. 5(a) and 5(b)]. For a thin film we expect grains with lateral dimensions comparable to the film thickness [32], and we expect platinum (atomic number $Z = 78$) to dominate STEM contrast relative to titanium ($Z = 22$). Clearly conventional STEM is imaging the thicker, heavier Pt layer in this bimetallic film. While some of the grain structure from Figs. 5(a) and 5(b) is evident in the STEM EBIC image [Fig. 5(c)], the STEM EBIC image is dominated by grain structure with a length scale of about 5 nm (i.e., the thickness of the titanium film). This equivalence indicates that Fig. 5(c) shows an image of the buried 5-nm Ti layer. Unlike in SEM SE imaging, STEM SEEBIC imaging detects SEs emitted from the bottom (beam exit) as well as the top (beam incident) surface of the sample. The SE yield of Pt is among the highest of the elements, and higher than that of Ti [27], so dominant Ti contrast in Fig. 5(c) suggests strong SE emission from the beam exit surface [33,34]. Alternatively, the strength of the Ti signal relative to that of Pt might be due to the generation of SEs by inner-shell excitation events [35], since for these Ti has a substantially larger cross section than Pt [36].

V. CONCLUSION

In conclusion, we demonstrate STEM SEEBIC imaging, which maps electronic properties such as connectivity and work function. Relative to standard EBIC imaging, SEEBIC imaging gives contrast even in electric-field-free regions of a sample. Relative to STEM with off-sample SE detectors, STEM SEEBIC imaging can provide a SE detection efficiency of unity, allowing direct measurement of net SE yield. Perhaps the most important distinction between STEM SEEBIC imaging and these related techniques, however, is the differential contrast illustrated in each of the double EBIC images in Fig. 2. Detecting the SEs and the associated holes with an integral part of the device itself enables precision mapping of, for instance, the conductance watershed as shown. In nanoelectronic devices such as resistive random-access memory, knowledge of the connectivity landscape is key to understanding device function [37]. This application will be explored in future work.

ACKNOWLEDGMENTS

[1] F. J. Garcia de Abajo, Optical excitations in electron microscopy, Rev. Mod. Phys. **82**, 209 (2010).

[2] M. Mecklenburg, W. A. Hubbard, E. R. White, R. Dhall, S. B. Cronin, S. Aloni, and B. C. Regan, Nanoscale temperature mapping in operating microelectronic devices, Science **347**, 629 (2015).

[3] T. E. Everhart, O. C. Wells, and R. K. Matta, A novel method of semiconductor device measurements, Proc. IEEE **52**, 1642 (1964).

[4] H. J. Leamy, Charge collection scanning electron microscopy, J. Appl. Phys. **53**, R51 (1982).

[5] K. V. Ravi, C. J. Varker, and C. E. Volk, Electrically active stacking faults in silicon, J. Electrochem. Soc. **120**, 533 (1973).

[6] J. I. Hanoka and R. O. Bell, Electron-beam-induced currents in semiconductors, Annu. Rev. Mater. Sci. **11**, 353 (1981).

[7] L. Pasemann, H. Blumtritt, and R. Gleichmann, Interpretation of the EBIC contrast of dislocations in silicon, Phys. Status Solidi (a) **70**, 197 (1982).

[8] C. V. Hari Rao, H. E. Bates, and K. V. Ravi, Electrical effects of SiC inclusions in EFG silicon ribbon solar cells, J. Appl. Phys. **47**, 2614 (1976).

[9] J. C. Manifacier and L. Szepessy, Efficient sprayed In$_2$O$_3$:Sn n-type silicon heterojunction solar cell, Appl. Phys. Lett. **31**, 459 (1977).

[10] K. Yamaguchi, N. Nakayama, H. Matsumoto, and S. Ikegami, CdS–CdTe solar cell prepared by vapor phase epitaxy, Jpn. J. Appl. Phys. **16**, 1203 (1977).

[11] J. D. Poplawsky, C. Li, N. R. Paudel, W. Guo, Y. Yan, and S. J. Pennycook, Nanoscale doping profiles within CdTe grain boundaries and at the CdS/CdTe interface revealed by atom probe tomography and STEM EBIC, Sol. Energy Mater. Sol. Cells **150**, 95 (2016).

[12] P. H. Rekemeyer, C. M. Chuang, M. G. Bawendi, and S. Gradecak, Minority carrier transport in lead sulfide quantum dot photovoltaics, Nano Lett. **17**, 6221 (2017).

[13] D. S. H. Chan, V. K. S. Ong, and J. C. H. Phang, A direct method for the extraction of diffusion length and surface recombination velocity from an EBIC line scan: Planar junction configuration, IEEE. Trans. Electron Devices **42**, 963 (1995).

[14] W. Shockley, Problems related to p-n junctions in silicon, Solid State Electron. **2**, 35 (1961).

[15] L. Reimer, *Scanning Electron Microscopy: Physics of Image Formation and Microanalysis* (Springer, Berlin, 1998), 2nd ed.

[16] V. E. Cosslett, D. Fathy, T. G. Sparrow, and U. Valdre, Investigation of semiconductor materials and devices by high voltage STEM techniques, Krist. Tech. **14**, 1177 (1979).

[17] K. L. Bunker, J. C. Gonzalez, D. Batchelor, T. J. Stark, and P. E. Russell, Development of a high lateral resolution electron beam induced current technique for electrical characterization of InGaN-based quantum well light emitting

diodes, MRS Online Proc. Libr. Arch. **743,** L10.10.1 (2002).

[18] E. R. White, A. Kerelsky, W. A. Hubbard, R. Dhall, S. B. Cronin, M. Mecklenburg, and B. C. Regan, Imaging interfacial electrical transport in graphene-MoS$_2$ heterostructures with electron-beam-induced-currents, Appl. Phys. Lett. **107,** 223104 (2015).

[19] M.-G. Han, J. A. Garlow, M. S. J. Marshall, A. L. Tiano, S. S. Wong, S.-W. Cheong, F. J. Walker, C. H. Ahn, and Y. Zhu, Electron-beam-induced-current and active secondary-electron voltage-contrast with aberration-corrected electron probes, Ultramicroscopy **176,** 80 (2017).

[20] R. F. Egerton, P. Li, and M. Malac, Radiation damage in the TEM and SEM, Micron Int. Wuhan Symp. Adv. Electron Microsc. **35,** 399 (2004).

[21] See Supplemental Material at http://link.aps.org/supplemental/10.1103/PhysRevApplied.10.044066 for supplementary figures.

[22] L. Reimer and H. Kohl, *Transmission Electron Microscopy: Physics of Image Formation*, Springer Series in Optical Sciences Vol. 36 (Springer, New York, NY, 2008), 5th ed.

[23] H. Inada, D. Su, R. F. Egerton, M. Konno, L. Wu, J. Ciston, J. Wall, and Y. Zhu, Atomic imaging using secondary electrons in a scanning transmission electron microscope: Experimental observations and possible mechanisms, Ultramicroscopy **111,** 865 (2011).

[24] M. S. Chung and T. E. Everhart, Simple calculation of energy distribution of low-energy secondary electrons emitted from metals under electron bombardment, J. Appl. Phys. **45,** 707 (1974).

[25] J. D. Jackson, *Classical Electrodynamics* (Wiley, New York, 1999), 3rd ed.

[26] J. G. Trump and R. J. Van de Graaff, The secondary emission of electrons by high energy electrons, Phys. Rev. **75,** 44 (1949).

[27] H. Seiler, Secondary electron emission in the scanning electron microscope, J. Appl. Phys. **54,** R1 (1983).

[28] J. Cazaux, Some considerations on the secondary electron emission, δ, from e^- irradiated insulators, J. Appl. Phys. **85,** 1137 (1998).

[29] J. Hölzl and Schulte, F. K. *Solid Surface Physics*, Springer Tracts in Modern Physics Vol. 85 (Springer, Berlin, 1979).

[30] R. Davies, Ph.D. thesis, Utah State University, Logan, UT, 1999.

[31] W. Chang, J. Dennison, J. Kite, and R. Davies, in *38th Aerospace Sciences Meeting and Exhibit, Reno, NV* (American Institute of Aeronautics and Astronautics, 2000).

[32] C. V. Thompson, Grain growth in thin films, Annu. Rev. Mater. Sci. **20,** 245 (1990).

[33] V. N. E. Robinson, The dependence of emitted secondary electrons upon the direction of travel of the exciting electron, J. Phys. D: Appl. Phys. **8,** L74 (1975).

[34] L. Reimer and H. Drescher, Secondary electron emission of 10–100 keV electrons from transparent films of Al and Au, J. Phys. D: Appl. Phys. **10,** 805 (1977).

[35] A. Howie, Recent developments in secondary electron imaging, J. Microsc. **180,** 192 (1995).

[36] R. D. Leapman, P. Rez, and D. F. Mayers, K, L, and M shell generalized oscillator strengths and ionization cross sections for fast electron collisions, J. Chem. Phys. **72,** 1232 (1980).

[37] W. A. Hubbard, A. Kerelsky, G. Jasmin, E. R. White, J. Lodico, M. Mecklenburg, and B. C. Regan, Nanofilament formation and regeneration during Cu/Al$_2$O$_3$ resistive memory switching, Nano Lett. **15,** 3983 (2015).